233 (2024) 212539

Contents lists available at ScienceDirect

Geoenergy Science and Engineering

journal homepage: www.sciencedirect.com/journal/geoenergy-science-and-engineering

Gravity drainage of bitumen under controlled thermodynamic conditions in DME-steam co-injection

Hassan Amer [a], Kai Sheng [a], Ryosuke Okuno [a,*], Abdullah Al-Gawfi [b], Petro Nakutnyy [c]

[a] The University of Texas at Austin, USA
[b] SaskEnergy, Canada
[c] Saskatchewan Research Council, Canada

ARTICLE INFO

Keywords:
Steam-assisted gravity drainage
Steam-solvent coinjection
Bitumen
Dimethyl ether
Small-scale experiment

ABSTRACT

Dimethyl ether (DME), a water-soluble solvent, has been studied as a potential additive to steam for improving the efficiency of steam-assisted gravity drainage (SAGD) for bitumen recovery. This paper presents an experimental study of bitumen gravity drainage in DME-SAGD in comparison to SAGD and butane-SAGD (C_4-SAGD).

Small-scale experiments were conducted using a sand pack with a diameter of 1.5 inches and a length of 15 inches, which was housed inside a 25-L cylindrical steel vessel. A DME-SAGD experiment with 10 mol% DME was conducted at 3500 kPa with a total in-situ injection rate of 3897 cm^3/min. Temperature distributions inside and outside the sand pack, as well as injection and production histories, were recorded during the experiment. Results were compared with previous studies of SAGD and C_4-SAGD (20 mol% C_4) that used the same experimental program. Then, numerical simulations were performed to history-match the experimental data and investigate the bitumen recovery mechanisms.

The peak bitumen rate was 16.8 cm^3/min for 10 mol% DME-SAGD, 9.8 cm^3/min for SAGD, and 14.6 cm^3/min for 20 mol% C_4-SAGD. That is, DME was more effective than C_4 as a steam additive even at the concentration reduced by half. The observed enhancement in bitumen drainage was attributed partly to the combined thermal and dilution effects on bitumen viscosity reduction, in which DME-SAGD exhibited a higher chamber-edge temperature than C_4-SAGD. Furthermore, the oleic (L) and aqueous (W) phases were more evenly distributed with less gravity segregation in the sand pack in DME-SAGD than in SAGD and C_4-SAGD, which facilitated the overall bitumen flow in the sand pack. Results collectively show that the slight polarity of DME as a solvent additive to steam enhanced the bitumen flow not only by L-phase viscosity reduction, but also by more uniformly enhanced bitumen flow in the sand pack.

1. Introduction

Dimethyl ether (DME) is a colorless non-toxic gas at standard conditions, liquefies under moderate pressure or cooling, and can be used in several applications such as petrol engines and turbines (Semelsberger et al., 2006; Lee et al., 1995; Fleisch et al., 1997). DME has its vapor pressure curve (i.e., volatility) between propane (C_3) and n-butane (C_4) (Ratnakar et al., 2016a). DME has been studied for several reservoir engineering applications such as waterflooding and heavy oil recovery.

Researchers at Shell presented DME-enhanced waterflooding (DEW) where DME was co-injected with brine to enhance oil recovery by waterflooding (Ratnakar et al., 2016a; Bakhsh et al., 2022). DME was first-contact miscible with oil and was partially soluble in water because of its polarity. The main oil recovery mechanisms for DEW were oil swelling and oil viscosity reduction (Ratnakar et al., 2016a). The co-injected DME could be recovered from the produced water, and the produced water containing DME could be recycled for re-injection (Parsons et al., 2016; Chernetsky et al., 2015). Mahdizadeh et al. (2019) used a calibrated numerical model based on a 1D coreflooding experiment to predict residual oil saturation as a function of DME concentration for DEW. Javanmard et al. (2019) performed a DEW coreflooding experiment with a fractured chalk plug. They showed that the oil swelling factor owing to DEW was 2.7 at reservoir conditions and was larger than other common solvents.

The phase behavior of DME-brine-oil mixtures plays a crucial role in controlling the mass transfer of DME between the aqueous and oleic

* Corresponding author. Center for Subsurface Energy and the Environment, 200 E. Dean Keeton Street, Stop C0300, Austin, TX, 78712, USA.
E-mail address: okuno@utexas.edu (R. Okuno).

https://doi.org/10.1016/j.geoen.2023.212539
Received 14 October 2023; Received in revised form 19 November 2023; Accepted 24 November 2023
Available online 30 November 2023

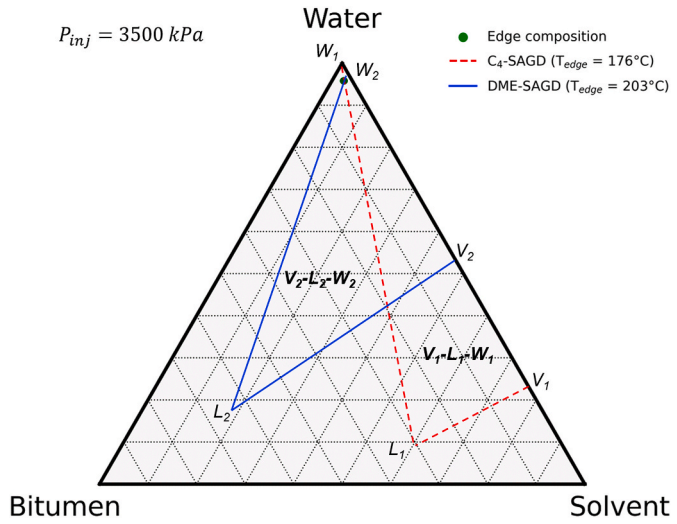

Fig. 1. A ternary diagram for water, solvent, and bitumen. The overall edge composition lies on the edge of each tie-triangle where a transition occurs from vapor (V), oleic (L), and aqueous (W) to L and W phases. The DME partitioning into the W phase results in a higher T_{edge} (blue line) compared to an alkane solvent with a similar volatility (C_4 in the red line). That is, $T^{sat}_{water} = T^{edge}_{SAGD}$ (solvent − free edge) $> T^{edge}_{DME-SAGD} > T^{edge}_{C_4-SAGD} > T^{3-phsae}_{water-solvent}$ (bitumen-free edge).

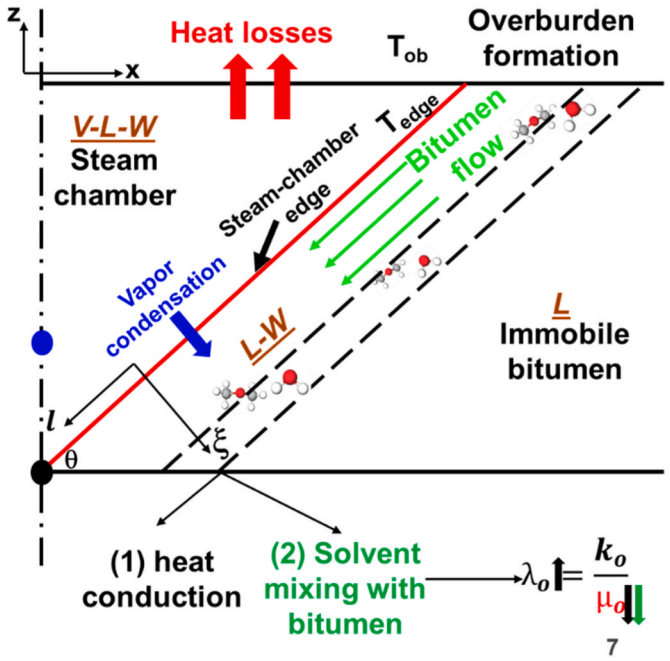

Fig. 2. A schematic diagram that depicts bitumen production in DME-SAGD. Bitumen viscosity decreases by means of heat and dilution in the gravity drainage zone. DME partitioning into the three phases is expected to enhance the mixing between DME and bitumen in the gravity-drainage zone.

phases. Phase behavior data were obtained for DME-hydrocarbon (Garcia-Sanchez et al., 1987; deFernández et al., 1992; Outcalt and Lemmon, 2013; Park et al., 2007; Haddadnia et al., 2018a) and DME-water (Pozo and Streett, 1984; Holldorff and Knapp, 1988) binary mixtures. Advanced equation of state (EOS) models were required to match the phase behavior data because of the partitioning of DME into water and hydrocarbon phases. Ratnakar et al. (2016a) used a cubic-plus-association EOS model based on Soave-Redlich-Kwong (Soave, 1972) to match phase behavior experimental data for DME-brine-live oil mixtures at reservoir conditions. Later, Ratnakar et al. (2016b) used the Peng-Robinson (PR) EOS (Robinson and Peng, 1978) with the Huron and Vidal (HV) mixing rules (Huron and Vidal, 1979) to match the DME partitioning coefficient data for DME-brine-live oil mixtures. Using the HV mixing rules with the PR EOS was advantageous because (1) the HV mixing rules reduce to the van der Waals mixing rules when the mixture contains no polar components and (2) commercial simulators are adaptive to use the HV mixing rules.

Discussing DME applications in bitumen recovery requires a general introduction of heavy oil recovery. Countries, such as Canada and Venezuela, have a significant amount of extra-heavy oil resources, also known as bitumen. Bitumen is extremely viscous, and it is not uncommon to show a viscosity above a million centipoise at ambient conditions. Since bitumen does not flow naturally at the initial reservoir conditions, thermal methods have been developed to reduce the viscosity of bitumen, thereby enhancing its flow. Examples of these methods include steam-assisted gravity drainage (SAGD) (Butler, 1985), in-situ combustion (Rodriguez et al., 2022, 2023), and solvent aided SAGD (SA-SAGD) (Nasr et al., 2003). SAGD involves injecting steam into a top horizontal well, where the steam condenses near the edge of a steam chamber, releasing the latent heat to the surrounding rock that contains bitumen. The resulting hot bitumen and water flow under gravity toward a bottom horizontal producer, typically situated 5 m below the injector (Al-Bahlani and Babadagli, 2009). In contrast, SA-SAGD involves the co-injection of a solvent with steam, which enhances bitumen drainage through both heat and dilution (Yang et al., 2021a). This paper is concerned with a type of SA-SAGD in which the solvent coinjected is DME.

Sheng et al. (2017) and Okuno (2018) were the first publications on co-injection of DME with steam for SAGD for bitumen recovery. Sheng et al. (2018) numerically studied a 2 mol% DME-SAGD and compared it with SAGD and C_4-SAGD, in which C_4 was an alkane solvent with a similar volatility to DME. The partitioning of DME into the oleic (L) and aqueous (W) phases increased the efficiency of bitumen recovery partly because the gravity segregation between oil and water was reduced, enhancing the mixing between bitumen and DME. Besides, DME had a higher solvent recovery than C_4 because the former tended to condense more than the latter from the steam chamber. Baek et al. (2019) subsequently conducted viscosity experiments for DME-bitumen mixtures using various concentrations of DME. They matched the viscosity data by fitting a modified Arrhenius equation. Furthermore, at a lower pressure of 1000 kPa, Haddadnia et al. (2018b) concluded that a 5 vol% DME-SAGD had a similar bitumen drainage effectiveness to C_4-SAGD after experimenting with a 2D model. Other authors studied DME in the context of the warm VAPEX process. Yang et al. (2021b) and Chai et al. (2022) showed that using warm DME-VAPEX increased bitumen

Table 1
Model parameters for bitumen's pseudo-components using PR-EOS. The PR-EOS model was calibrated with the measured bitumen PVT data using Kumar and Okuno's (Kumar and Okuno, 2016) method.

	Mol %	MW, g/mol	T_c, °C	P_c, kPa	Acentric factor (ω)
B1	49.5	283.0	526.35	2000	0.3996
B2	50.5	831.1	976.62	1314	0.8712

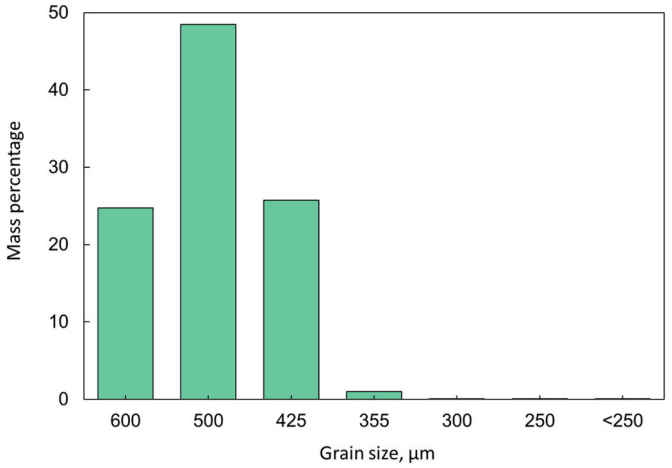

Fig. 3. Sieve analysis results as a grain size distribution (expressed in mass percentage) of the sand pack with an average grain size of 500 μm.

Table 2
Measured properties for the sand pack used in SAGD and 10 mol% DME-SAGD experiments, including pore volume, porosity, initial water saturation, and permeability.

Case \Property	Pore volume, cm^3	Porosity, %	Initial water saturation, %	Permeability, D
SAGD	519.1	33.2	7.2	76
10 mol% DME-SAGD	522.3	33.0	8.3	76

recovery in comparison to SAGD because of the DME's enhanced mass transfer by partitioning into L and W phases.

Based on the previous studies, DME's potential to enhance the efficiency of bitumen recovery comes fundamentally from its partitioning into the three phases, vapor (V), oleic (L), and aqueous (W) phases, which is expected to affect the thermodynamic conditions near the edge of a steam chamber (Sheng et al., 2017) and in turn affect the characteristics of flow and mixing in the mobile-bitumen zone. Therefore, this research is focused on an experimental study of DME-SAGD with a small-scale sand pack surrounded by a void space for which the pressure and overall composition are controlled by a steady-state vapor flow. The experimental program systematically follows Amer et al. (2024), who studied SAGD and co-injection of steam with hydrocarbon solvents (butane, octane, and condensate), but not DME. Use of the same experimental program as Amer et al. (2024) enables a consistent comparison between DME-SAGD, C_4-SAGD, and SAGD.

To make the introduction to DME-SAGD more specific to the focus of this research requires further explanation about the effect of water-soluble solvent on the edge of a steam chamber. Fig. 1 shows the tie triangles for two ternary systems, water-DME-bitumen and water-C_4-bitumen, at 3500 kPa when the overall composition, 97 mol% water, 2 mol% solvent, and 1 mol% bitumen, is on the W-L edge of the tie triangle. The temperature so defined is the chamber-edge temperature (T_{edge}) when the phase transition between V–W-L and W-L (i.e., complete condensation of vapor) occurs for the assumed overall composition at 3500 kPa. Each tie triangle is attached to three two-phase zones, although they are not shown for clarity in Fig. 1. The phase behavior for water-DME-bitumen was calculated using a calibrated PR EOS (Robinson and Peng, 1978) with the HV mixing rules from Sheng et al. (2017). For water-C_4-bitumen, phase behavior was based on a calibrated PR EOS with the van der Waals mixing rules (Venkatramani and Okuno, 2015; Kumar and Okuno, 2016). Then, T_{edge} was calculated at 203°C for water-DME-bitumen and 176°C for water-C_4-bitumen for this illustrative example. The solvent partitioning in the W phase (DME here) tends to shift the tie-triangle to the left toward the solvent-free binary edge. This left edge essentially corresponds to the saturation temperature of water at 3500 kPa, which is 241°C, and represents the upper bound of T_{edge} where bitumen has negligible vapor pressure. The bitumen-free binary edge (right) corresponds to the three-phase temperature of the water-solvent mixture and serves as the lower bound for T_{edge}. That is, $T^{sat}_{water} = T^{edge}_{SAGD}$ (solvent − free edge) $> T^{edge}_{DME-SAGD} > T^{edge}_{C_4-SAGD} > T^{3-phase}_{water-solvent}$ (bitumen-free edge). Therefore, DME co-injection is expected to result in a higher T_{edge} compared to an alkane solvent, such as butane, at the same conditions. Keshavarz et al. (2014, 2015) presented this type of analysis for hydrocarbon solvents, but not for DME.

Fig. 2 schematically shows how bitumen flows under the gravity for DME-SAGD. The injector and producer are horizontal wells that are typically several meters apart. DME is co-injected with steam as a single-phase vapor into the upper injector. The steam chamber is supposed to expand laterally in the target formation upon reaching the top boundary (Region 1). Water and DME condense out of the vapor phase along the steam-chamber edge. The steam condenses into hot water and the latent heat of condensation transfers to rock and fluids in the gravity drainage zone (Region 2). DME condenses and mixes with bitumen in the L phase, but also through the interface between the W and L phases in the gravity drainage of W and L in the solvent-bitumen mixing zone (Region 2). Moreover, DME-SAGD exhibits a higher T_{edge} than C_4-SAGD as explained with Fig. 1 and Sheng et al. (2017, 2018).

As described above, the main difference between DME and hydrocarbon solvent as an additive to steam comes fundamentally from the thermodynamic conditions at the edge of a steam chamber. Therefore, this research used the experimental procedure that controls the pressure and overall composition in the vapor phase surrounding the sand pack in which bitumen drainage occurs, as presented by Sheng et al. (2022a) and Amer et al. (2024) for SAGD and hydrocarbon solvents. We show a systematic set of experimental data for 10 mol% DME-SAGD and compare them with the data from SAGD (Amer et al., 2024) as the control experiment. Besides the experimental data on temperature readings and bitumen production rate, this paper presents a detailed analysis of flow characteristics in the sandpack using history-matched simulations. Unlike previous studies, the novelty of this research lies in the comprehensive investigation of DME-SAGD in comparison to SAGD by both experiments and calibrated numerical models. Note again that this research is focused on the effect of thermodynamic conditions near the chamber edge on bitumen drainage; that is, it is not intended to mimic the transient behavior of bitumen recovery by SAGD at field conditions.

In the following sections, the experimental method and results are presented first. Following this, the simulation history-matching procedure, results, and analysis are discussed. Finally, the main conclusions are summarized.

2. Experimental methods

2.1. Materials

2.1.1. Bitumen properties

The bitumen sample used in both SAGD and DME-SAGD experiments

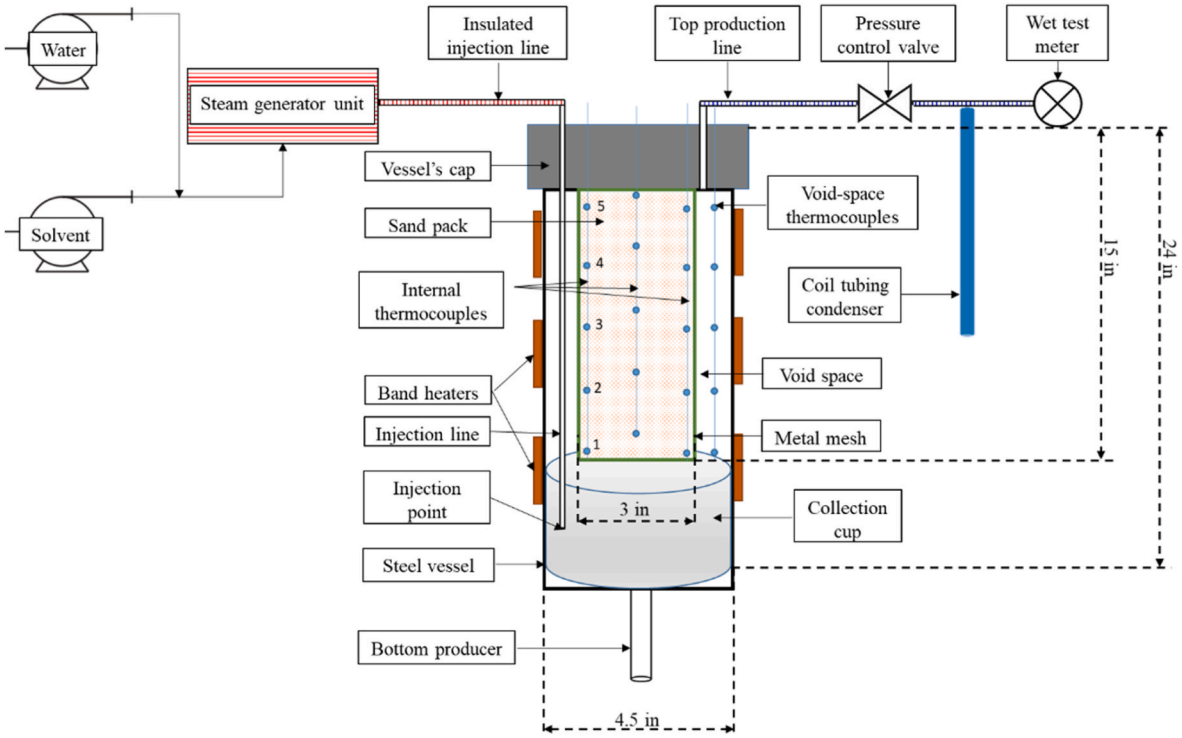

a) A side view of the experimental setup with labels for the main components

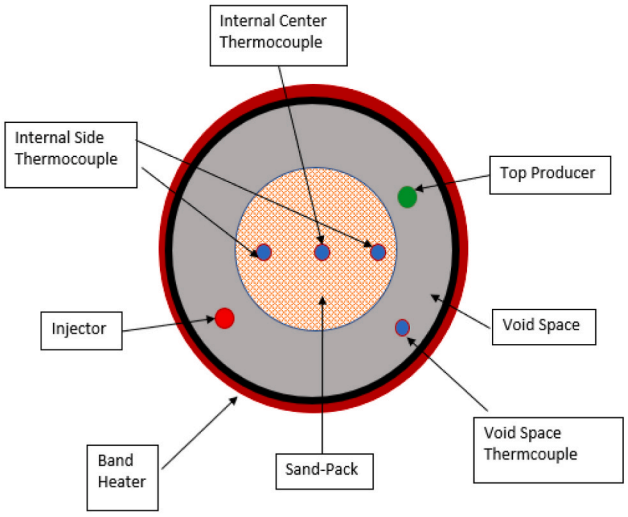

b) A top view of the experimental setup

Fig. 4. A schematic depicting the small-scale experimental vessel utilized in this study. Steam and solvent were co-injected into the void space away from the sand pack through an injection port at the end of the line. The top production line, regulated by a pressure control valve, maintained the vessel's pressure at 3500 kPa by venting excess vapor. Meanwhile, the lower production line was connected to the collection container to recover the liquids. Twenty temperature sensors were distributed inside the vessel, with five sensors per thermocouple (TC) line. These TC lines encompassed three within the sand pack and one in the void space.

came from an operation site in Alberta, and its molecular weight was 560 g/mol. The SARA (Saturate, Aromatic, Resin, and Asphaltene) analysis gave 18% asphaltenes, 19% saturates, 39% aromatics, 18% resins, and 6% unrecovered. The mass density of the bitumen sample at 101.3 kPa was 1015 kg/m^3 at 15 °C, 999 kg/m^3 at 40°C, and 974 kg/m^3 at 80°C. The viscosity of the bitumen sample at 101.3 kPa was 10^6 cp at 15°C, 24,000 cp at 40°C, and 675 cp at 80°C.

The bitumen was characterized using two pseudo-components, B1 (distillable) and B2 (non-distillable), with a calibrated Peng-Robinson EOS model (Gao et al., 2017). The vapor pressure properties (e.g., P_C, T_C, and ω) for these pseudo-components were estimated following Kumar and Okuno's method (Kumar and Okuno, 2016), as shown in Table 1. Furthermore, models for bitumen's density and viscosity were developed by matching the experimental data, as elaborated in Section 4.

2.1.2. Sand properties and packing

The porous medium used in this research was an unconsolidated

Table 3
Injection rates and saturation temperatures for SAGD and DME-SAGD experiments. The steam pump unit operated at 3500 kPa and 22°C, whereas the solvent pump unit operated at 2500 kPa and 7°C. The injection fluid was 100% vapor above the saturation temperature. The total in-situ injection rate was the same for both experiments to ensure steady-state flow inside the void space region.

	Saturation temperature, °C	Steam injection rate at pump conditions (CWE), cm^3/min	Solvent injection rate at pump conditions, cm^3/min	Total injection rate at in-situ conditions, cm^3/min
SAGD	241	70.00	0.00	3987
10 mol% DME-SAGD	234	62.36	26.27	3987

Table 4
Components of phases in the bottom production stream in the DME-SAGD experiment as a basis for material balance calculations.

Phase	Component(s)
Vapor (*V*)	DME
Oleic (*L*)	DME, bitumen, and water
Aqueous (*W*)	Water

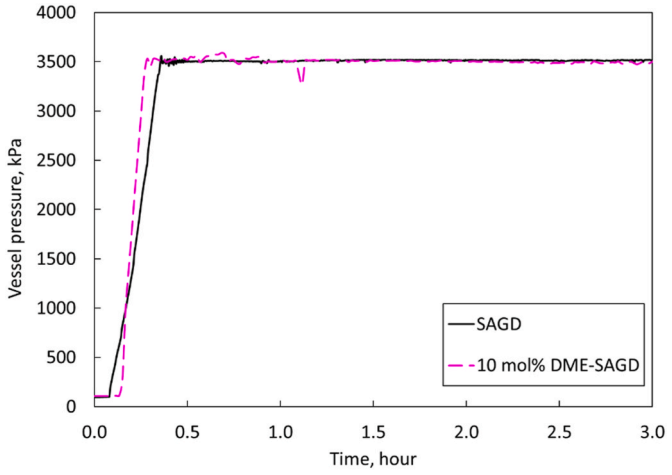

Fig. 5. Vessel's pressure histories for the SAGD and the 10 mol% DME-SAGD experiments. The pressure inside the vessel was kept at 3500 kPa after the void space temperature reached the saturation temperature of each experiment (Table 3) after approximately 19 min.

sand pack with a diameter of 7.6 cm and a height of 38.1 cm. The average bulk volume was 1579 cm^3, and the pore volume was 521 cm^3. The mineral composition was primarily quartz. Fig. 3 shows the grain size distribution for the sand pack, with an average grain size of 500 μm. The grain size distribution was determined through a sieve analysis process. Larger mesh sizes were specifically chosen to suppress capillary-dominated flow in the experiment.

Preceding each experiment, the sand was manually transferred to the apparatus and compacted in place using vibrating hammers. Deionized water was then used to fully saturate the sand pack and to measure the porosity (0.33) and permeability (76 D) at 22°C. Following this, heated bitumen at 70°C was injected and displaced the deionized water. Table 2 summarizes the measured physical properties of the sand pack for SAGD and 10 mol% DME-SAGD experiments. Importantly, both sand packs had the same permeability because the same batch of sand was used throughout the experiments. The physical properties of the sand pack were maintained by refraining from transferring the sand between the measuring devices and the drainage apparatus. Instead, all measurements were conducted with the sand packed within the original

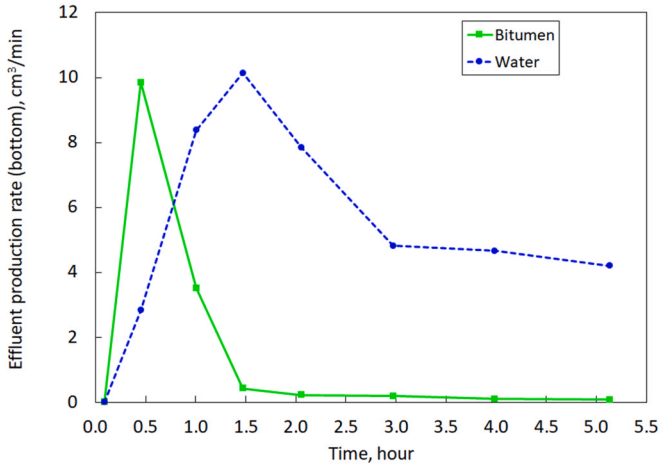

(a) SAGD experiment

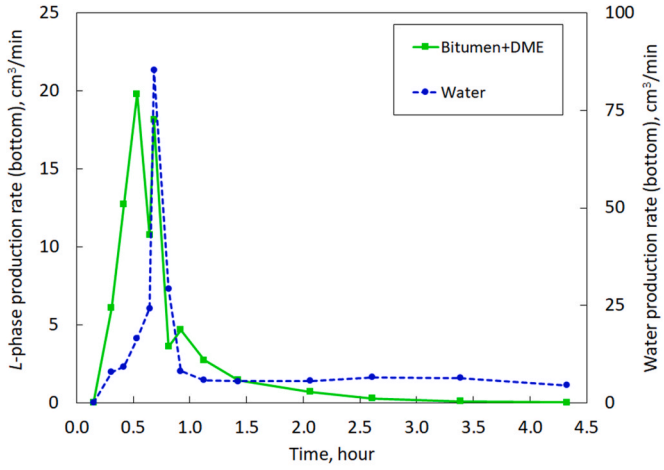

(b) 10 mol% DME-SAGD experiment

Fig. 6. Effluent production history for (a) SAGD and (b) 10 mol% DME-SAGD experiments. The green line represents the L phase history, which consisted of bitumen only (for SAGD) and bitumen and DME (for DME-SAGD). The water rate peaked after the L phase. For the 10 mol% DME-SAGD, the L phase exhibited two peak rates; the second peak rate coincided with the water peak rate because of the mutual solubility of DME.

Table 5
The material balance calculations for the SAGD experiment.

	Total water injected, cm^3	Total water produced, cm^3
	21400	20737
Difference	+663	3.1%

Table 6
The material balance calculations for the 10 mol% DME-SAGD experiment.

	Total water injected, cm^3	Total water produced, cm^3	Total DME injected, cm^3	Total DME produced, cm^3
	15777	16190	6594	6010
Difference	−413	−2.6%	+584	8.9%

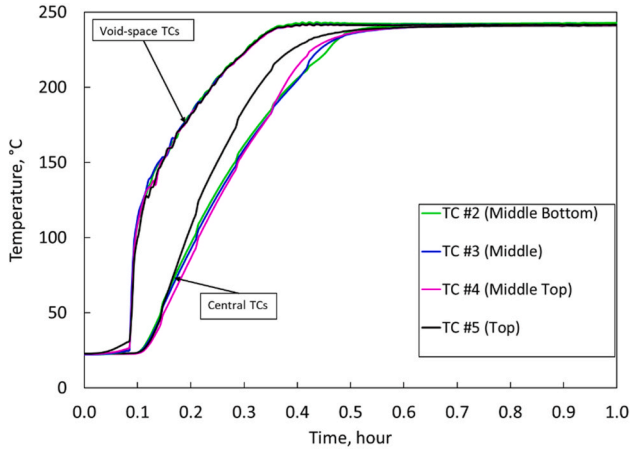

(a) Temperature reading histories for SAGD experiment.

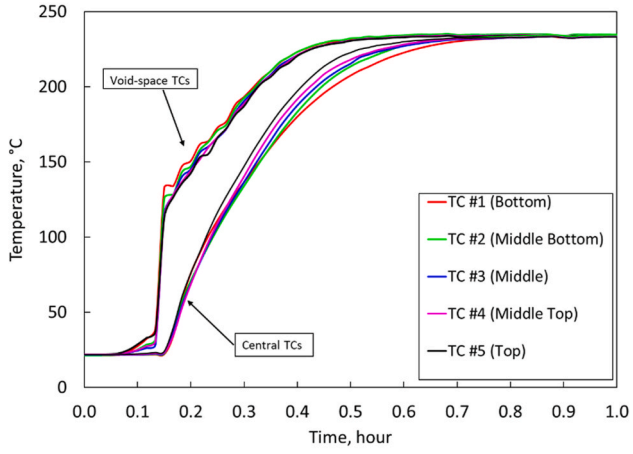

(b) Temperature reading histories for the 10 mol% DME-SAGD experiment.

Fig. 7. Temperature reading histories as obtained from both the void-space thermocouples (TCs) and central TCs within the sand pack for (a) SAGD and (b) 10 mol% DME-SAGD experiments. Specifically, "TC #5″ and "TC #1″ represent the top and bottom thermocouples, respectively.

apparatus.

2.2. Experimental setup

Fig. 4a is a schematic side view of the experimental setup with labels for the main components, and Fig. 4b is the top view. The vessel was a 25-L steel cylinder with an outer diameter of 11.4 cm and a length of 60.9 cm. A sand pack was placed inside the top portion of the steel vessel. Then, the sand pack was wrapped in a thin steel mesh (screen), attached to the vessel's cap, and secured in place. The vessel's cap was a metal end that screwed into the steel vessel. The offset distance between the sand pack and the interior side wall of the steel vessel created a 3.8-cm annular void space. The vessel was surrounded by band heaters that provided the required heat during the experiment. The bottom portion of the steel vessel included a 20.3 cm-long collection cup that laterally extended to the interior side wall of the vessel.

The steel vessel had one inlet and two outlets. The inlet was an insulated injection line, with the upstream side connected to the steam generator and pump units and the downstream side connected to an injector. The injector was a port that was placed inside the collection cup and oriented towards the inner wall of the steel vessel, away from the sand pack. This injection configuration was to avoid the direct injection of fluids into the sand pack.

The first outlet was the top production line, with a top producer on the upstream side and a pressure control valve, a wet test meter, and a coil tubing condenser on the downstream side. The fluids produced from the top production line were 100% vapor, which was separated into DME and water components using a rotary evaporator (rotovap) for the DME-SAGD experiment.

The second outlet was the liquid discharge line, with the collection cup on the upstream side and a bottom producer on the downstream side. The effluent (water, solvent, and bitumen) accumulated in the collection cup during the experiment and was collected by turning on and off the bottom valve. These bottom samples were collected frequently under in-situ conditions using a 300-mL "sample loop" that was connected to the bottom valve. Then, the sample was transferred from the sample loop to a vial for volume measurement and separation of each component.

Five outer band heaters surrounded the steel vessel to control heat losses to the surroundings. Moreover, the vessel comprised 20 sensors for temperature measurement during the experiment, and they were mounted on four thermocouple (TC) lines, each containing five sensors. Within the sand pack, three TC lines were embedded–two on each side and one in the center–along with one TC line in the void space region (Fig. 4a).

The experimental setup included the following pieces of equipment:

- Two syringe pumps: Isco 500D and Isco 1000D, rated at a maximum operating pressure of 34.0 MPa.
- A 15-kW steam generator unit operating at 480 V.
- A flow control valve equipped with a digital-to-analog control system.
- Five band heaters, with the top two providing 360 W at 208 V and the bottom three supplying 2.0 kW at 208 V.
- A stainless-steel condenser linked to a glycol chiller.
- A drum-type gas meter capable of measuring a maximum flow rate of 900 L/h.
- Four sets of TC lines, each containing 5 temperature sensors.

2.3. SAGD and DME-SAGD experiments

The essential data obtained for 10 mol% DME-SAGD and SAGD experiments were histories of vessel pressure, effluent production (top and bottom), and temperature distribution in the sand pack and the surrounding void space. The thermodynamic conditions in the vapor phase in the test vessel were set for DME-SAGD by specifying the pressure at 3500 kPa and the overall composition of 10 mol% DME and 90 mol% water. Then, T_{edge} was estimated as the condensation temperature of the specified overall composition and pressure by using the PR EOS, as shown in Sheng et al. (2022b). Multiple preliminary experiments and numerical simulations were performed to ensure that a steady state in vapor composition and temperature could be achieved at the total injection rate of 3987 cm^3/min for SAGD and DME-SAGD. This rate corresponded to 70 cm^3/min of steam (expressed as cold-water equivalent,

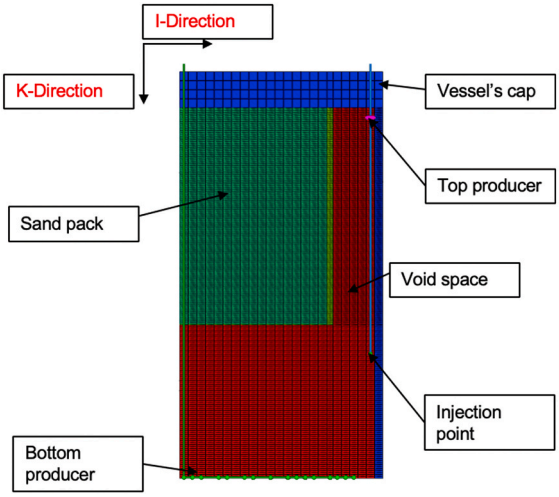

a) 2D vertical section of the simulation model. Only half of the symmetrical model is shown with a scale of 0.2:1.

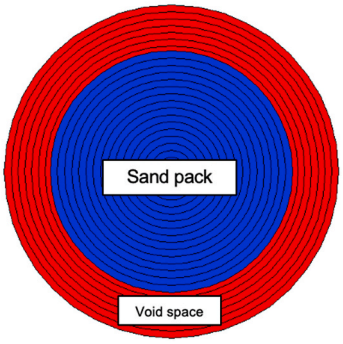

b) 2D top planar view of the simulation model.

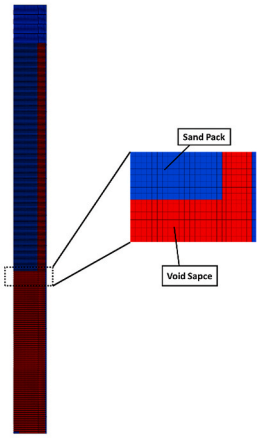

c) A visualization for the simulation model using a scaling ratio of 1:1.

Fig. 8. A numerical model for the small-scale experimental setup. The model consisted of two regions: the sand pack and the void space.

CWE) for the SAGD experiment at pump conditions (with a pressure of 101 kPa and a temperature of 22°C). For the 10 mol% DME-SAGD experiment, the water and DME injection rates were calculated from the total injection rate of 3897 cm^3/min. Table 3 provides a summary of the water and DME injection rates under pump conditions, saturation temperature, and total injection rate under in-situ conditions for both the SAGD and DME-SAGD experiments.

The SAGD experimental procedure was based on Amer et al. (2024), who presented a SAGD and five SA-SAGD experiments (20 mol% C_4, 40 mol% C_4, 10 mol% C_8, 20 mol% C_8, and 10 mol% condensate). Here, we present the DME-SAGD experiment to investigate how the partitioning of DME into the three phases would impact the bitumen gravity drainage compared to SAGD. The experimental procedure is summarized as follows:

Step 1: Inject nitrogen (N_2) gas to fill up the annular void space inside the steel vessel. The injection stream later displaced the N_2 gas, which was produced through the top production line.

Step 2: Preheat the steel vessel for 5 min by turning on the outer band heaters. There were five band heaters surrounding the steel vessel.

Step 3: Adjust the temperature of the band heaters to 5°C above the saturation temperature for each experiment (Table 3). This step controlled heat losses and maintained the temperature inside the vessel

Table 7
Parameters for the Stone I relative permeability model after history-matching the SAGD experiment, based on Amer et al. (2024).

Inputs to Stone I model	Value
S_{wr}	0.07
S_{orw}	0.23
S_{org}	0.23
S_{gr}	0
k_{ro0}	1
k_{rw0}	0.05
k_{rg0}	1
n_w	3.0
n_o	1.9
n_g	3.0

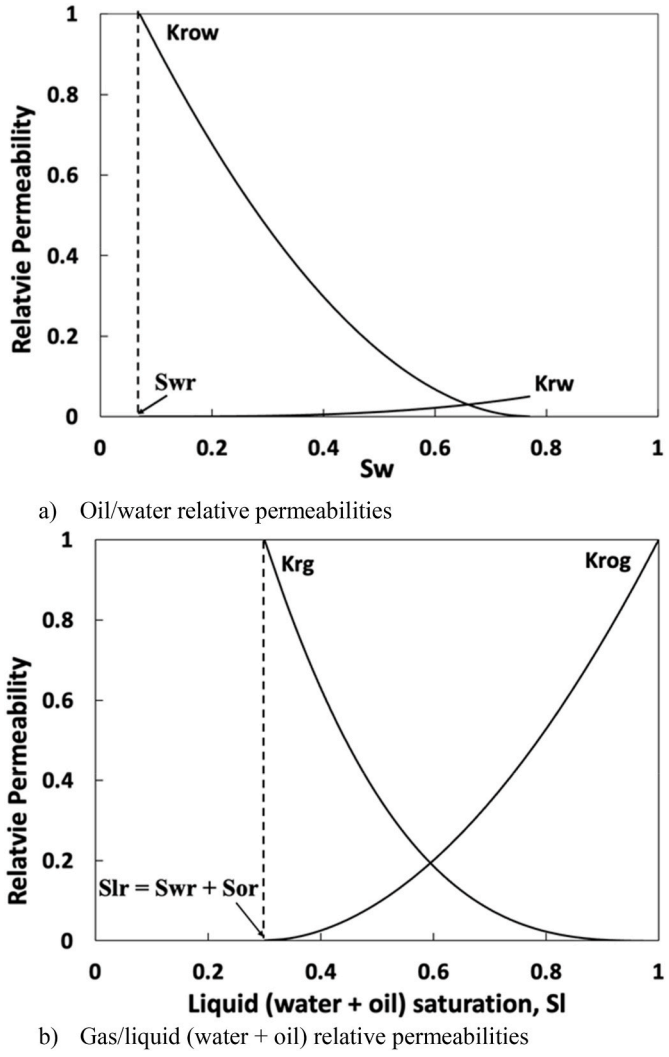

Fig. 9. Relative permeability curves used for SAGD and 10 mol% DME-SAGD simulations.

as per the design.

Step 4: For SAGD, inject steam at 70 cm^3/min (cold-water equivalent, CWE) at a temperature of 241°C. This injection rate corresponded to a total in-situ injection rate of 3897 cm^3/min at 3500 kPa (target pressure), as outlined in Table 3, to ensure steady-state conditions in the annular space. For DME-SAGD, the liquid DME was transferred from the DME pump to the steam generator unit for co-injection with steam.

Step 5: Gradually increase the steam (and solvent, for DME-SAGD) pump pressure by 200 kPa per minute until the vessel's pressure reaches 3500 kPa (target pressure).

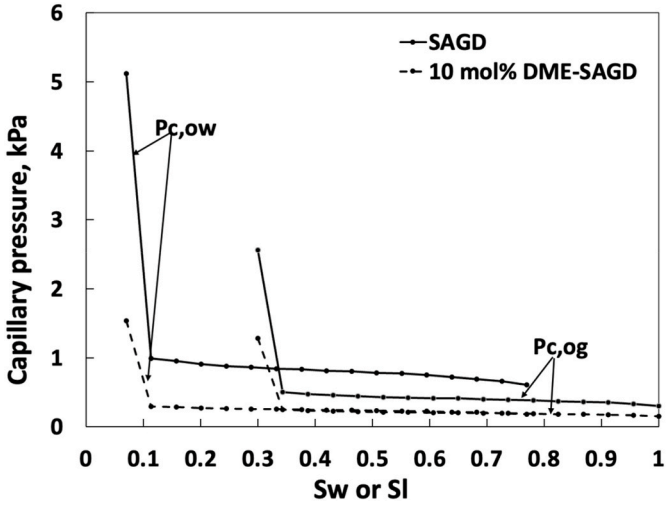

Fig. 10. Capillary pressure curves used for the SAGD and the 10 mol% DME-SAGD simulations.

Step 6: The pressure control valve automatically operates to maintain the vessel's pressure at 3500 kPa by producing the excess vapor through the top production line.

Step 7: Begin collecting the produced liquid sample from the bottom production line once the vessel's pressure reaches the target pressure of 3500 kPa. Note that the DME-SAGD experiment had a higher sample collection frequency compared to SAGD. Specifically, eight samples were collected for DME-SAGD, whereas for SAGD, four samples were only taken during the first hour. During the sample collection, the bottom valve was turned on, and the vessel's pressure profile exhibited momentary pressure drops that lasted for 1–5 min.

Step 8: Following the final drainage period, turn off the outer band heater and stop fluid injection. Allow the vessel to pressurize and cool down before recovering the sand pack for Dean-Stark analysis. The SAGD experiment lasted for 5 h, whereas the DME-SAGD experiment lasted for 4 h because DME-SAGD was so effective that bitumen drainage occurred more rapidly than SAGD.

The main differences between the SAGD and DME-SAGD experiments included the following:

- The DME pump operated at 7°C and 3500 kPa and transferred the liquid DME into the steam generator unit for co-injection (Step 4).
- DME-SAGD had a higher sample collection frequency, twice that of SAGD, during the first hour of production.
- The produced streams from the top and bottom lines underwent additional separation for DME, water, and bitumen components.

In the DME-SAGD experiment, component separation was conducted for both the top and bottom production streams. The top production stream primarily consisted of a single-phase vapor comprising water and DME components, which were separated using the rotovap technique. In contrast, the bottom production stream included three phases (V, L, and W). Table 4 provides an overview of the component distribution within these phases, facilitating material balance calculations. Specifically, the V phase was considered 100% DME because the water vapor was assumed to be produced entirely from the top line. The W phase was designated as 100% water, referred to as free water, because DME was assumed to have negligible solubility in the W phase at ambient conditions. Meanwhile, the L phase encompassed three components: DME, bitumen, and water. Toluene was added to the L phase to separate the dissolved water. Notably, the separation of DME from bitumen in the L phase presented significant technical challenges, consistent with prior

Table 8
Water-oil and oil-gas interfacial tensions used for the SAGD and 10 mol% DME-SAGD history-matching simulations. IFT values for the 10 mol% DME-SAGD were based on the calibrated numerical model. Compared to the 20 mol% C_4-SAGD, the 10 mol% DME-SAGD had significantly lowered IFTs due to the partitioning into the three phases.

Case	Water-oil IFT (σ_{ow}), dynes/cm	Oil-gas IFT (σ_{og}), dynes/cm	Reference
SAGD	30	15	(Sheng et al., 2021)
20 mol% C_4-SAGD	18	4.5	(Amer et al., 2024)
10 mol% DME-SAGD	9	2.25	This research (calibrated numerical model)

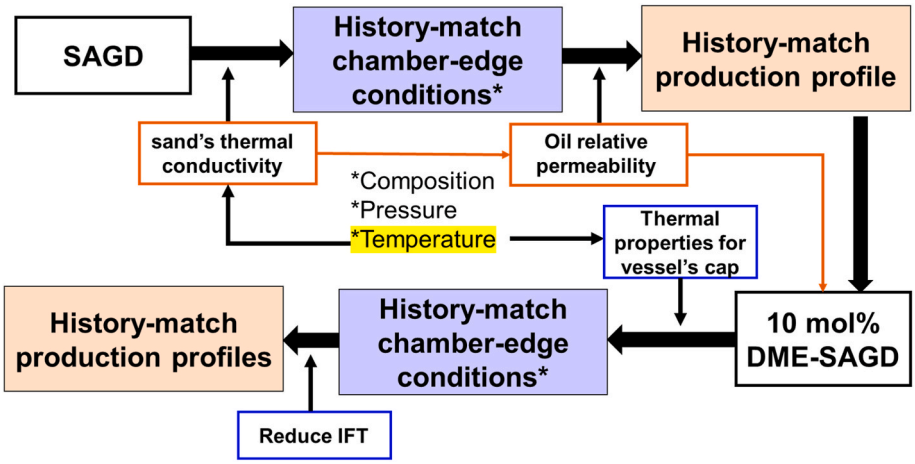

Fig. 11. Graphical abstraction for the flow chart of the history matching procedure in Appendix A.

research findings (Pratama et al., 2021). To calculate the total amounts of water and DME produced in the DME-SAGD experiment, the following two equations were employed, respectively:

$$m_{water}^{produced,total} = m_{water,V\ phase}^{produced,top} + m_{water,L\ phase}^{produced,bottom} + m_{water,W\ phase}^{produced,bottom}$$

$$m_{DME}^{produced,total} = m_{DME,V\ phase}^{produced,top} + m_{DME,V\ phase}^{produced,bottom}$$

In these equations, $m_{i,j}^{produced,k}$ represents the mass of component i within phase j produced in stream k.

3. Experimental results

This section presents the results of both the SAGD and 10 mol% DME-SAGD experiments, including the vessel's pressure profiles, effluent production histories, material balance calculations, and temperature profiles inside and outside the sand pack. Fig. 5 illustrates the vessel's pressure profiles for these two experiments. The pressure was gradually increased and stabilized at 3500 kPa as soon as the void space temperature reached the saturation temperature for each experiment (Table 3). Notably, the saturation temperature varied between the two experiments, leading to different ramp-up durations of 17 and 21 min for the SAGD and 10 mol% DME-SAGD experiments, respectively. The vessel's pressure stabilization was achieved by venting excess vapor through the top production line, effectively controlling thermodynamic conditions, particularly pressure, near the steam-chamber edge.

Fig. 6a illustrates the effluent production history (by component) for the SAGD experiment. In this case, the L phase consisted only of bitumen because water was separated by adding toluene. Bitumen production began at 0.09 h after steam injection, reaching a peak rate of 9.84 cm^3/min before declining. Notably, the water peak rate experienced a delay due to the lack of volatile components in the system, as the experiments utilized dead bitumen. Fig. 6b presents the effluent production history (by component) for the 10 mol% DME-SAGD experiment. Unlike SAGD, the L phase in this case consisted of both DME and bitumen (Table 4). The L phase rate history exhibited two distinct peak rates. The second peak rate occurred concurrently with the water peak rate, attributable to the mutual solubility of DME in the L and W phases. The first L phase peak rate was 19.83 cm^3/min, followed by the second at 18.16 cm^3/min. Although the effluent data were used for calibrating the numerical model, the comparison between SAGD and DME-SAGD in bitumen drainage rate had to rely on the history-matched numerical simulations, as will be shown later, because the L phase in DME-SAGD contains DME (Table 4).

Tables 5 and 6 present a summary of the material balance calculations conducted for both the SAGD and 10 mol% DME-SAGD experiments. The material balance error percentage is defined as follows:

Material balance error percentage for component i $(MBE\%)_i$ = [(cumulative volume injected)$_i$ – (cumulative volume produced)$_i$]/(cumulative volume injected)$_i$.

In both experiments, the water material balance error remained below 3%. However, for the DME-SAGD experiment, the DME had the largest material balance error of 8.9% because the DME could not be entirely separated from the produced L phase.

Fig. 7 displays the temperature data recorded by the five thermocouples (TCs) placed at different locations along each TC line for both experiments. Note that, for simplicity, we showed only temperature readings from the void space and central TC lines. The results revealed a rapid increase in void space temperatures immediately after injection began, increasing them from the initial room temperature of 21°C to the specified saturation temperature for each experiment (Table 3).

Furthermore, the central TCs exhibited a lower rate of temperature increase in comparison to the void space TCs because of the lower thermal conductivity of the sand pack. Then, the central TCs recorded temperatures similar to those of the void space TCs. This transition in flow regime enabled the observation of transient conditions within the sand pack through temperature and fluid-production data, in conjunction with history-matched numerical simulations.

Both experimental cases demonstrated qualitatively similar temperature profiles along the central axis of the cylindrical sand pack. The steam chamber, containing steam and solvent in the vapor phase, progressed downward within the sand pack from top to bottom. The readings from the central TCs within the sand pack indicated that this

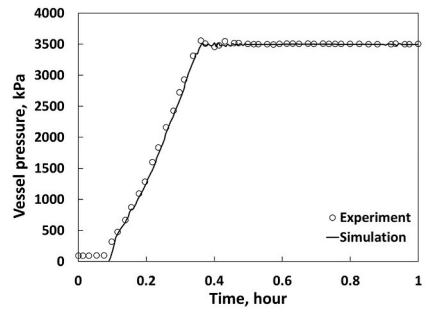

a) Pressure comparison profiles

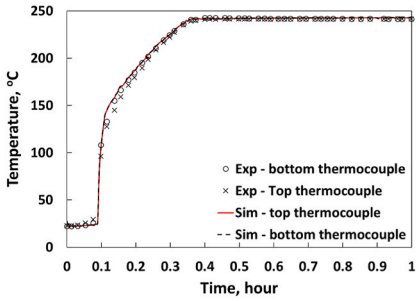

b) Void space (top and bottom) temperature profile comparison. The top and bottom TCs recorded similar temperatures of 241°C after 0.35 hours, which the simulation was able to match.

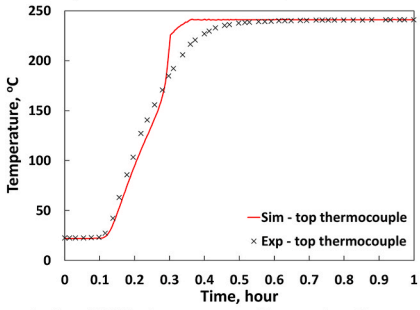

c) Central TC (top) temperature profile comparison. Temperature readings from the bottom central TC were not recorded during the experiment.

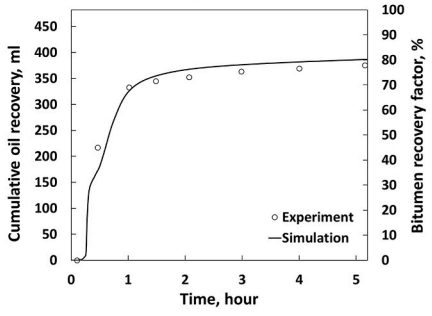

d) Bitumen material balance comparison. The measured ultimate RF of bitumen was 78%.

Fig. 12. Comparison results between simulation and experiment for the SAGD case. To provide a clearer visualization, experimental data for pressure and temperature were plotted every 0.02 h.

downward movement resulted in heat conduction, as illustrated in Fig. 7.

4. Simulation model and history matching

4.1. Simulation model

The thermal compositional simulator of Computer Modelling Group (CMG, 2020), STARS, was used to conduct compositional flow simulations, where phase behavior was modeled by K values. The numerical model of the experimental setup was based on Amer et al. (2024) and Sheng et al. (2022a), allowing for a systematic comparison between this research on DME and their studies on hydrocarbon solvents.

Fig. 8 provides an overview of the vertical and horizontal cross-sections of the numerical model, with dimensions representing the experimental setup (Fig. 4). The *I:K* scaling ratio of 0.2:1 was selected to conveniently display 2D maps from the numerical simulation in the subsequent figures. The void space encompassed the sand pack, which was surmounted by the vessel's cap. The model adopted a cylindrical coordinate system, where *I*, *J*, and *K* denote the horizontal, radial, and vertical directions, respectively. Comprising 5400 grid blocks, the model had 24 grid blocks in the *I* direction, each with a thickness of 0.22 cm per cylindrical ring; no discretization in the J direction; and 225 grid blocks in the *K* direction, with a grid size of 0.25 cm within the sand pack and 0.35 cm within the void space. This finer resolution within the sand pack controlled truncation errors during the simulation of transient flow related to steam chamber advancement, a key aspect of this small-scale experiment.

The numerical model incorporated three wells for injection and production (bottom and top). The injector was in the grid block (23, 1, 163) in the void space beneath the sand pack, with a constant in-situ injection rate of 3897 cm^3/min and an injection temperature of 241°C. This temperature exceeded the saturation temperature for each experiment (Table 3), ensuring that injected fluids remained in the vapor phase during simulation, representing the actual experimental conditions. The bottom producer was in the bottom layer and perforated across all the grid blocks from (1, 1, 225) to (23, 1, 225). This configuration guaranteed effective production of all the liquids when the bottom producer was active without significant accumulation in the vessel. The vessel's pressure readings (Fig. 8) served as the pressure constraints for the bottom producer. The top producer, situated in the upper portion of the void space at grid block (23, 1, 11), utilized the pressure gauge readings from the flow control valve as inputs. Similarly to the physical experiment, the top producer continuously vented the excess vapor, maintaining the vessel's pressure at 3500 kPa.

The sand pack had a porosity of 0.33 and a permeability of 76 D, which represented average values from measurements across the two experiments. The void space had a porosity of 0.999 and a permeability of 999 D, the maximum values permissible in the simulator. The outer cylindrical layer within the simulation served to model the vessel's band heater, while the top four layers represented the vessel's cap. These grid blocks had zero porosity and permeability, allowing no flow but permitting heat transfer. The band heater had a thermal conductivity of 20 J/(cm × min × °C), corresponding to stainless steel. The minute-by-minute averages of the void space temperature readings were used as the temperature inputs for the grid blocks representing the band heater. The numerical model was initialized based on the fluid saturations (water and oil) as directly measured for each experiment.

The fluid model used four components, which were water, DME, and two bitumen components, "distillable" B1 and "non-distillable" B2. To account for DME partitioning into the three phases for DME-SAGD simulations, two sets of K value tables (V-L and L-W) were generated based on the calibrated PR EOS with the HV mixing rules from Sheng et al. (2018).

The L phase consisted of bitumen and DME, with its density calculated using the ideal mixing assumption within STARS. The L phase's viscosity was calculated using the modified Arrhenius model within STARS.

The Stone I model was used to calculate the three-phase relative permeability within STARS **(Table 7).** Those parameters were obtained from Amer et al. (2024), who history-matched the SAGD experiment using the same experimental setup. Fig. 9 depicts the oil-water and gas-liquid relative permeability curves, respectively. These curves were obtained after history-matching the SAGD case, as explained in the following subsection. Furthermore, Fig. 10 shows the capillary pressure curves employed for the SAGD and SA-SAGD cases, respectively. The determination of capillary pressure was based on the grain size distribution (Fig. 3) and the Young-Laplace equation, assuming a bundle of

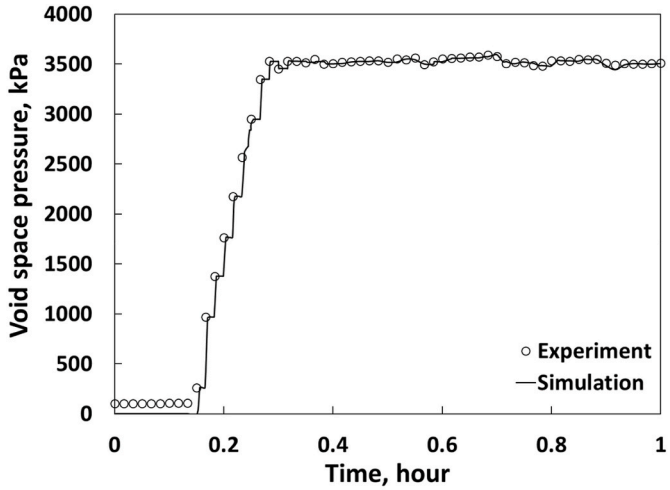

a) Pressure profile

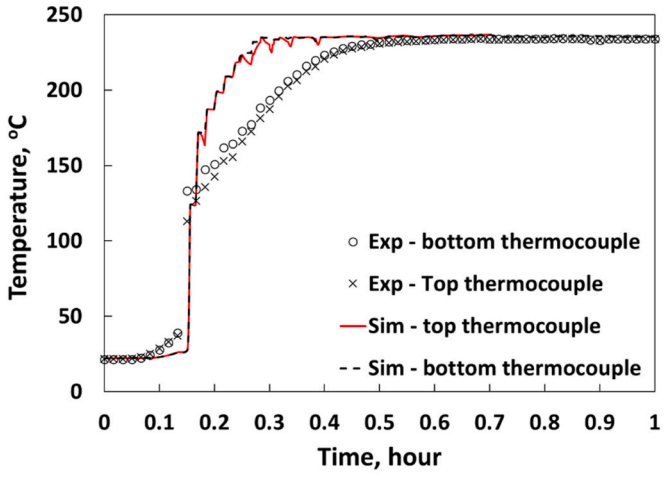

b) Void space temperature profile comparison

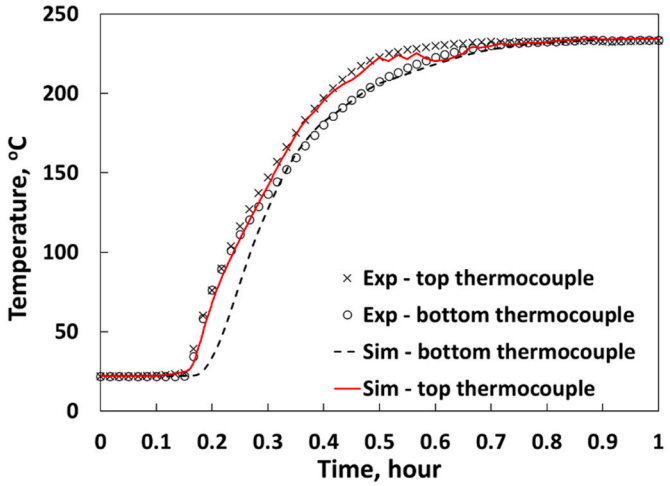

c) Central TC temperature profile comparison

Fig. 13. Comparison results between simulation and experiment for the 10 mol% DME-SAGD case.

capillary tubes (Sheng et al., 2022b). Table 8 summarizes the interfacial tensions (IFT) for water/oil (σ_{ow}) and oil/gas (σ_{og}) for the SAGD case and the 10 mol% DME-SAGD simulations. These differences in IFT values arise from the partitioning of the DME into the three phases, resulting in reduced IFTs for DME-SAGD (Pratama et al., 2020).

The thermal conductivities of the water, oil, and gas phases were set at 0.36, 0.072, and 0.02 J/(cm × min × °C), respectively. These thermal parameters remained unaltered during history-matching. Additionally,

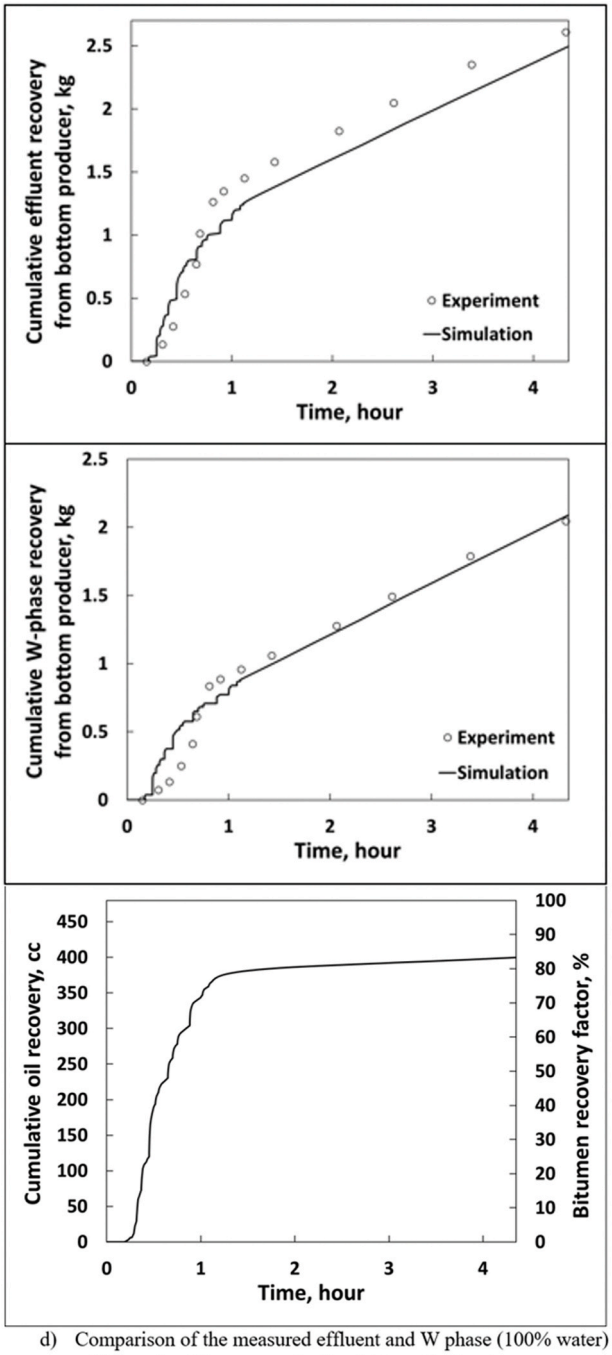

d) Comparison of the measured effluent and W phase (100% water) production histories to simulation. In addition, the bitumen production history (bottom) was generated based on the calibrated numerical model and was not directly measured during the experiment. The ultimate recovery factor of bitumen was 83% based on simulation.

Fig. 13. (*continued*).

the thermal conductivity of the vessel's cap was set at 5 J/(cm × min × °C), based on Amer et al. (2024). The vessel's cap was made of multiple steel pieces assembled through either point contacts or surface contacts, such as threads and riveting. The cap was also wrapped with other materials to reduce heat loss. All these contributed to the lowered heat conductivity. Finally, the sand pack's compressibility remained constant at 1.21×10^{-5} kPa^{-1}, a value obtained from prior research (Sheng et al., 2022a) using the same sand sample under similar thermodynamic conditions.

4.2. History matching procedure and results

For consistency, the history-matching procedure followed Amer et al. (2024). The main experimental data were temperature and material balance histories. Experimental data for SAGD were history-matched first. Subsequently, the SAGD's history-matched parameters served as the basis for the DME-SAGD simulation. Readings from void space TCs (top and bottom) and the sand pack central TCs (top, middle, and bottom) were compared against simulated temperature profiles. Appendix A shows a flowchart for the history-matching procedure in this research. Fig. 11 presents a schematic diagram for the history-matching procedure.

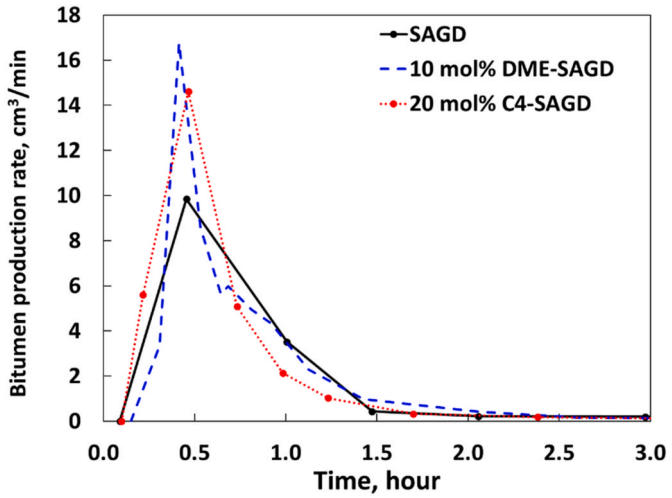

Fig. 14. Bitumen production rate history for SAGD, 20 mol% C_4-SAGD, and 10 mol% DME-SAGD cases. The history for the 10 mol% DME-SAGD case was based on the calibrated numerical model in this research, whereas the history for the 20 mol% C_4-SAGD case was based on Amer et al. (2024).

Table 9
Bitumen peak production rate, and total time to total recovery for SAGD, 20 mol % C_4-SAGD, and 10 mol% DME-SAGD.

Case	Bitumen peak rate, cm^3/min	Time to total recovery, hours
SAGD	9.84	5.05
10 mol% DME-SAGD	16.77	4.35
20 mol % C_4-SAGD (Amer et al., 2024)	14.61	4.78

For SAGD, the chamber-edge temperature was matched first by adjusting the sand's thermal conductivity to 1.5 J/(cm × min × °C), and then the bitumen material balance was matched by adjusting the oil relative permeability curve (using an exponent of 1.9 for calculating the k_{ro} curve from the oil-water relative permeability table). The adjusted parameters from the SAGD history-matching were used as inputs for DME-SAGD simulations. Similarly, for the 10 mol% DME-SAGD, the chamber-edge temperature was matched first by adjusting the vessel's cap thermal conductivity to 5 J/(cm × min × °C). Then, the L-W and L-V IFTs were lowered to match the effluent material balance (Table 8). This reduction in IFTs with DME-SAGD in contrast to SAGD was not unique to the current study; similar observations were made by Pratama and Babagadli (Pratama and Babadagli, 2020) in their 7 mol% DME-SAGD experiment, Zhao et al. (2023) in their experiments where kerosene was mixed with DME-brine mixtures, and Lee et al. (2021) in their simulation studies.

Fig. 12a–d and 13a-d compare the experimental data with the simulation results for SAGD and 10 mol% DME-SAGD. For both cases, the material balance for injection fluid (water for SAGD and water/DME for 10 mol% DME-SAGD) was perfectly history-matched; hence, their comparison plots are not shown for brevity. A reasonable match was achieved for the vessel pressure profile and temperature readings from the void space and central TCs. Note again that the complete separation of DME from the produced fluids was not done for the 10 mol% DME-SAGD experiment; therefore, the history matching relied on effluent (water + DME + bitumen) and water production data. The bitumen production profile for DME-SAGD (Fig. 13d) was generated based on the calibrated numerical model.

The ultimate recovery factors were 78% for SAGD and 83% for 10 mol% DME-SAGD. However, the focus of this research was on oil production rates under gravity drainage; that is, oil recovery factors in this experimental program do not represent transient mechanisms in SAGD because the thermodynamic conditions in the vapor phase were set on purpose.

Fig. 14 shows the history of the bitumen production rates for SAGD, 10 mol% DME-SAGD (based on the calibrated numerical model), and 20 mol% C_4-SAGD (based on Amer et al., 2024). The 10 mol% DME-SAGD case had the highest peak bitumen production rate of 16.77 cm^3/min. This rate was 70% greater than that of SAGD and 15% higher than 20 mol% C_4-SAGD. Table 9 provides a summary of the peak bitumen production rate and the time required for total bitumen recovery across the three cases. The 10 mol% DME-SAGD case required the shortest time, 4.35 h, for total bitumen production among the three cases. Importantly, DME-SAGD was more effective than C_4-SAGD, although the concentration of C_4 in C_4-SAGD was twice greater than the concertation of DME in DME-SAGD.

5. Discussion

The previous section showed that 10 mol% DME-SAGD was more effective than 20 mol% C_4-SAGD in enhancing bitumen gravity drainage at the same operating pressure. This section gives a detailed analysis of the results through local details using 2D maps from the calibrated numerical model and overall flow regime.

Fig. 15 shows the 2D maps used for the analysis in this section for SAGD, 20 mol% C_4-SAGD, and 10 mol% DME-SAGD. The 2D maps were generated at a timestep when the steam chamber reached the 20th layer in the z-direction inside the sand pack (20–27 min after the injection). The 2D maps for 20 mol% C_4-SAGD were generated based on the calibrated numerical model from Amer et al. (2024). The black rectangle inside the 2D maps represents one-half of the sand pack and demarcates between the sand pack and the void space regions. Fig. 15a exhibits the gas saturation maps for SAGD, C_4-SAGD, and DME-SAGD. Grid blocks with non-zero gas saturation represent the steam chamber. The steam chamber size inside the sand pack was the same for all the cases, for a consistent comparison of the three cases.

Fig. 15b shows the temperature distributions for the three cases. The steam chamber-edge temperature (T_{edge}) was the highest for SAGD and the lowest for the 20 mol% C_4-SAGD (i.e., $T^{edge}_{SAGD} > T^{edge}_{DME-SAGD} > T^{edge}_{C_4-SAGD}$) as expected from the phase behavior model (Fig. 1). Solvent-steam co-injection lowers T_{edge}; however, the co-injected solvent condenses and dilutes the bitumen (Amer et al., 2024). The dilution decreases the bitumen's viscosity and increases its mobility inside the gravity-drainage zone ahead of the steam chamber. Therefore, 20 mol% C_4-SAGD and 10 mol% DME-SAGD enhanced the bitumen drainage rate in comparison to SAGD.

Fig. 15c shows the 2D maps for the solvent mole fraction in the L phase for 20 mol% C_4-SAGD and 10 mol% DME-SAGD. The solvent concentration in the L phase near the chamber edge was three to four times greater in 20 mol% C_4-SAGD than that in 10 mol% DME-SAGD, which was also expected in Fig. 1.

Fig. 15d shows the DME mole fraction in the W phase away from the chamber edge. Unlike C_4, DME is a polar solvent and soluble in L and W phases. The partitioning of DME into L and W phases (a) results in a lower L-W IFT in DME-SAGD than SAGD (Pratama et al., 2020; Pratama and Babadagli, 2020) and C_4-SAGD (Table 8), and (b) reduces gravity segregation between the L and W phases as described in the numerical study of Sheng et al. (2018).

The grid-scale Bond numbers (N_b) based on the vapor in the annulus were calculated to characterize the resulting flow regime owing to gravity and interfacial forces using the following equation:

$$N_b = \frac{(\rho_o - \rho_g) g r^2}{\sigma_{og}} \times 10^{-3}$$

where ρ_g is the V-phase mass density, ρ_o is the L-phase mass density, σ_{og} is the L-V interfacial tension, g is the gravitational constant, and r is the

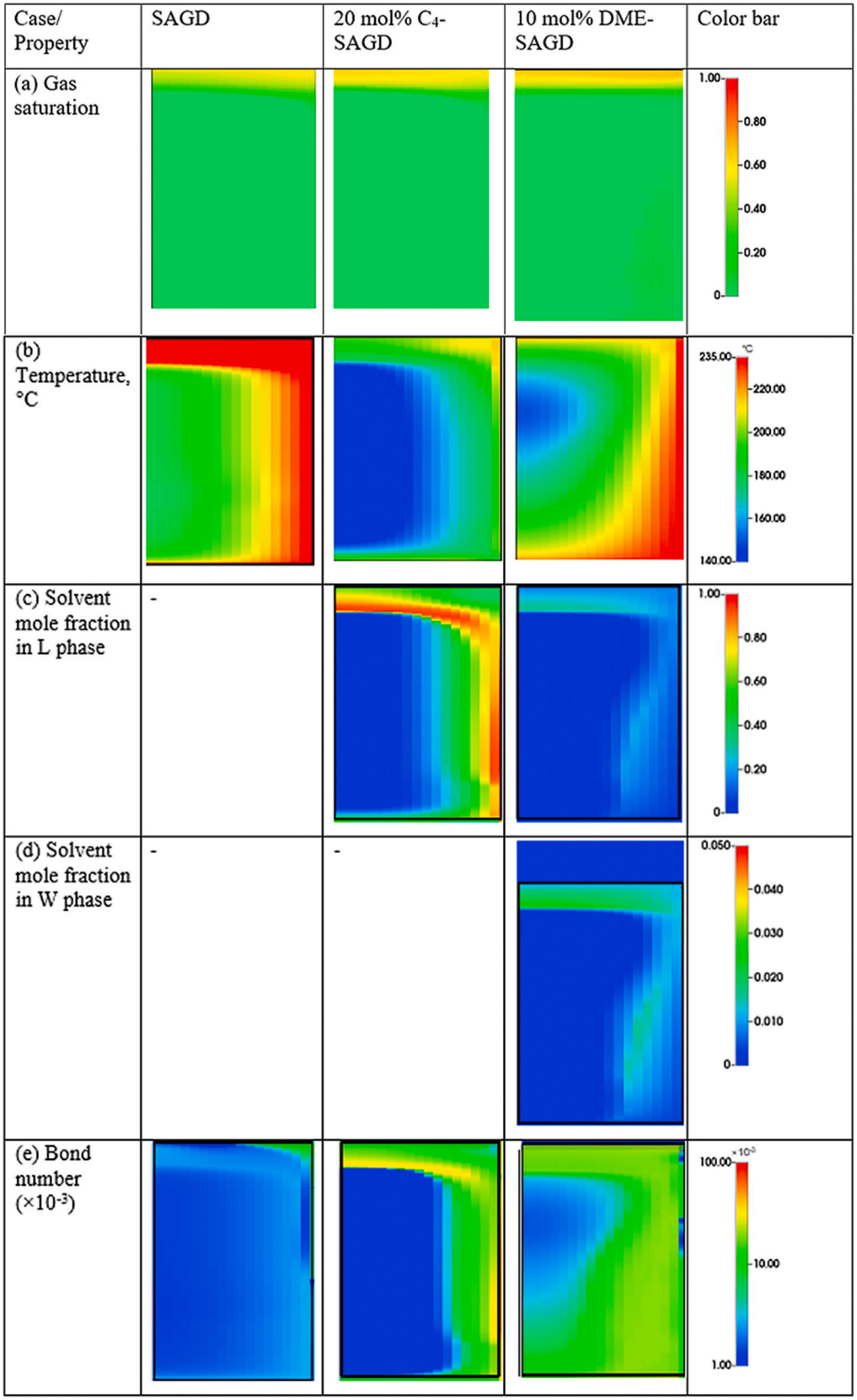

Fig. 15. 2D maps for SAGD, 20 mol% C_4-SAGD, and 10 mol% DME-SAGD. The timestep at which the cases were analyzed ranged from 20 to 27 min, or when the steam chamber reached the 20th layer in the z-direction. The color bar on the 4th column denotes the minimum and maximum values of the property displayed within each row besides its unit, if dimensional.

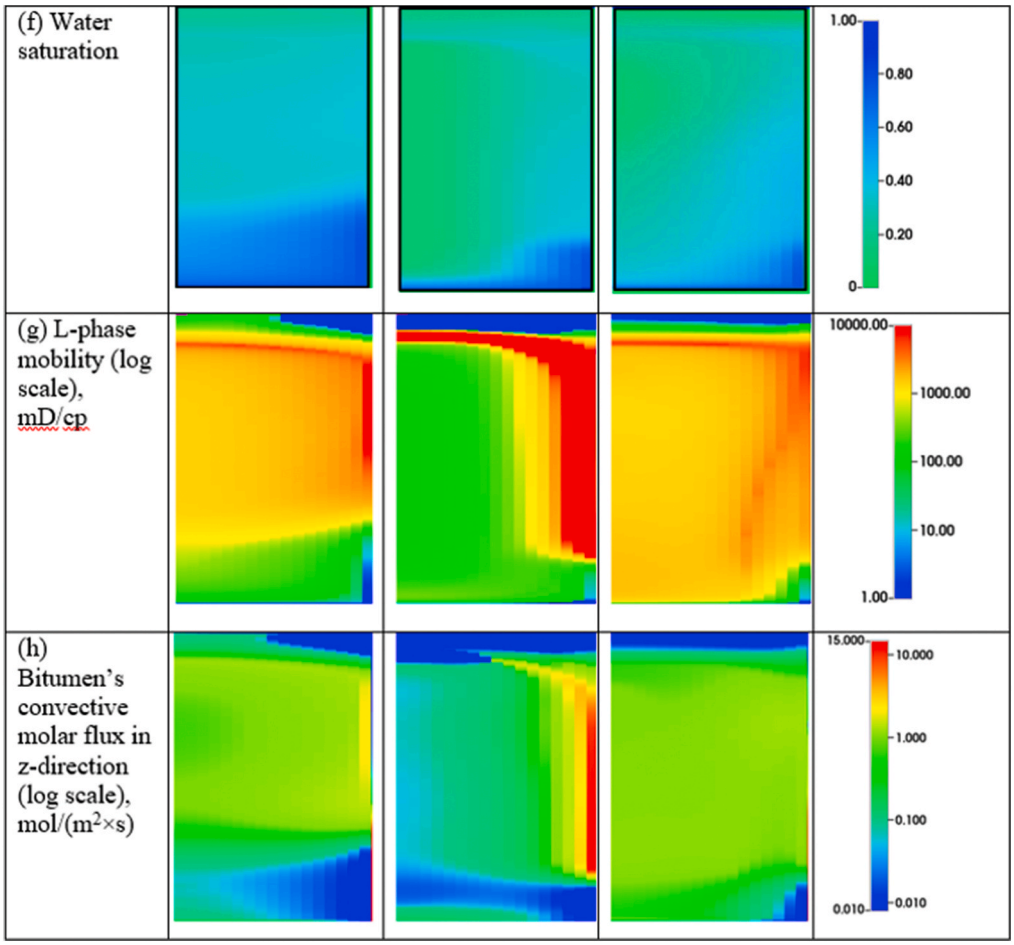

Fig. 15. (*continued*).

Table 10
Average L phase mobility for SAGD, 20 mol% C_4-SAGD, and 10 mol% DME-SAGD cases. A harmonic average was used for the grid blocks in the z-direction, and then an arithmetic average for the grid blocks in the x-direction.

Case	Overall L-phase mobility ($\lambda_{L,\ avg}$), D/cp
SAGD	0.23
20 mol% C_4-SAGD	0.72
10 mol% DME-SAGD	1.12

average pore size of 500 μm. For gravity drainage of bitumen, a greater N_b is desirable (Stewart et al., 2018). Fig. 15e clarifies that 10 mol% DME-SAGD resulted in a more uniformly enhanced N_b in the sand pack among the three cases.

Also, the three cases resulted in different distributions of the W and L phases. Fig. 15f shows W-phase distributions for SAGD, C_4-SAGD, and DME-SAGD. The W phase saturation increased from top to bottom in SAGD and 20 mol% C_4-SAGD cases; however, it was more evenly distributed with less gravity segregation for 10 mol% DME-SAGD. The more uniform distribution of L and W phases in DME-SAGD tended to facilitate the overall bitumen flow in the sand pack as shown in L-phase relative mobilities (Fig. 15g). This highlights the significant impact of phase distributions in the mobile bitumen zone on the gravity drainage of bitumen.

Fig. 15g indicates the important difference between C_4 and DME as a steam additive in the gravity drainage of bitumen. The condensed C_4 tends to accumulate in the vicinity of the steam-chamber edge at lower temperatures (Fig. 15b), whereas DME tends to enhance the bitumen flow more broadly and uniformly. The difference is attributed to the polarity of DME as a solvent additive to steam that causes the elevated temperature at the steam-chamber edge and the more uniform phase distribution.

A useful parameter to illustrate the above-mentioned point is the overall L-phase mobility ($\lambda_{L,\ avg}$) for the entire sand pack. We used a harmonic average for the grid blocks in the z-direction, and then an arithmetic average for the grid blocks in the x-direction (Peters, 2012). Table 10 shows that $\lambda_{L,\ avg}$ was 1.12 D/cp for 10 mol% DME-SAGD, which was greater than both 20 mol% C_4-SAGD of 0.72 and SAGD of 0.23 D/cp. The calculated $\lambda_{L,\ avg}$, based on calibrated numerical models, were consistent with measured bitumen production rates for these cases (Fig. 14).

Further analysis was performed using the convective molar flux of bitumen ($J_{C,bit}$) which directly indicates the effectiveness of bitumen drainage for SA-SAGD as follows:

$$J_{C,bit} = \xi_L x_{bit,L} \upsilon_L,$$

where ξ_L is the L-phase molar density, $x_{bit,L}$ is the bitumen molar fraction in the L phase, and υ_L is the L-phase interstitial velocity. Fig. 15h shows the $J_{C,bit}$ distribution for SAGD, C_4-SAGD, and DME-SAGD. The 20 mol% C_4-SAGD case had three orders of magnitude greater $J_{C,bit}$ distribution in the narrow zone of gravity drainage than 10 mol% DME-SAGD because of the solvent concentration distributions shown in Fig. 15c. Results collectively show that DME-SAGD tends to yield a more uniform enhancement of bitumen flow than C_4-SAGD.

6. Conclusions

This paper presents experimental data on bitumen gravity drainage under controlled thermodynamic conditions for DME-SAGD in comparison to SAGD and C_4-SAGD. The experimental data (temperature readings and material balance histories) were analyzed by calibrated numerical simulation models. The main conclusions are as follows:

1. The peak bitumen rate in gravity drainage was 16.8 cm^3/min for 10 mol% DME-SAGD, 9.8 cm^3/min for SAGD, and 14.6 cm^3/min for 20 mol% C_4-SAGD. That is, DME was more effective than C_4 as a steam additive, even when the concentration was reduced by half.
2. The mutual solubility of DME in L and W phases led to a more uniform phase distribution with less gravity segregation in the sand pack in comparison to SAGD and C_4-SAGD. The observations were quantitatively confirmed in different ways, such as overall L-phase mobility and bitumen molar flux in the sand pack. For example, the overall L-phase mobility was 1.22 D/cp for 10 mol% DME-SAGD, 0.72 D/cp for 20 mol% C_4-SAGD, and 0.23 D/cp for SAGD.
3. The enhanced bitumen drainage in 10 mol% DME-SAGD was attributed to the combined thermal and dilution effects on L-phase viscosity and also to the more uniform distribution of phases in the sand pack. The fundamental cause of these mechanisms is the slight polarity of DME as a solvent additive to steam, which results in a higher temperature near the steam-chamber edge and a more widely spread influence of condensed solvent in the mobile bitumen zone.

CRediT authorship contribution statement

Hassan Amer: Data curation, Formal analysis, Investigation, Methodology, Validation, Visualization, Writing - original draft. **Kai Sheng:** Data curation, Formal analysis, Investigation, Methodology, Validation, Visualization, Writing - review & editing. **Ryosuke Okuno:** Conceptualization, Formal analysis, Funding acquisition, Investigation, Methodology, Project administration, Resources, Supervision, Validation, Writing - original draft, Writing - review & editing. **Abdullah Al-Gawfi:** Conceptualization, Data curation, Formal analysis, Investigation, Methodology, Validation, Writing - review & editing. **Petro Nakutnyy:** Conceptualization, Data curation, Formal analysis, Funding acquisition, Investigation, Methodology, Project administration, Resources, Supervision, Validation, Writing - review & editing.

Declaration of competing interest

The authors declare that they have no known competing financial interests or personal relationships that could have appeared to influence the work reported in this paper.

Data availability

Data will be made available on request.

Acknowledgements

This research was performed as part of the Energi Simulation Industrial Affiliate Program on Carbon Utilization and Storage (ES Carbon UT) at the Center for Subsurface Energy and the Environment at the University of Texas at Austin. Ryosuke Okuno holds the Pioneer Corporation Faculty Fellowship in Petroleum Engineering at the University of Texas at Austin.

Nomenclature

ρ	Density, kg/m^3
ω	Acentric factor
λ	Phase mobility, D/cp
φ	Porosity
σ	Interfacial tension, dynes/cm
ν	Interstitial velocity, m/s
ξ	Molar density, mol/m^3
J_C	Convective molar flux, mol/(m^2.s)
k_{row}	Oil relative permeability for oil/water relative permeability table
k_{rog}	Oil relative permeability for gas/liquid relative permeability table
N_b	Bond number
S_{rl}	Residual liquid saturation
S_{wr}	Residual water saturation
S_{orw}	Residual oil saturation for oil-water relative permeability curve
S_{org}	Residual oil saturation for liquid-gas relative permeability curve
S_{gr}	Residual gas saturation
n_w	Exponent for water relative permeability
n_o	Exponent for oil relative permeability
n_g	Exponent for gas relative permeability
r	Diameter of pore size, μm

Abbreviations

CMG	Computer Modelling Group
DME-SAGD	Dimethyl ether-Aided Steam-Assisted Gravity Drainage
EOS	Equation of State
SAGD	Steam-Assisted Gravity Drainage
SA-SAGD	Solvent-Aided Steam-Assisted Gravity Drainage

Appendix A. Flow Chart for SAGD and DME-SAGD History Matching Procedure

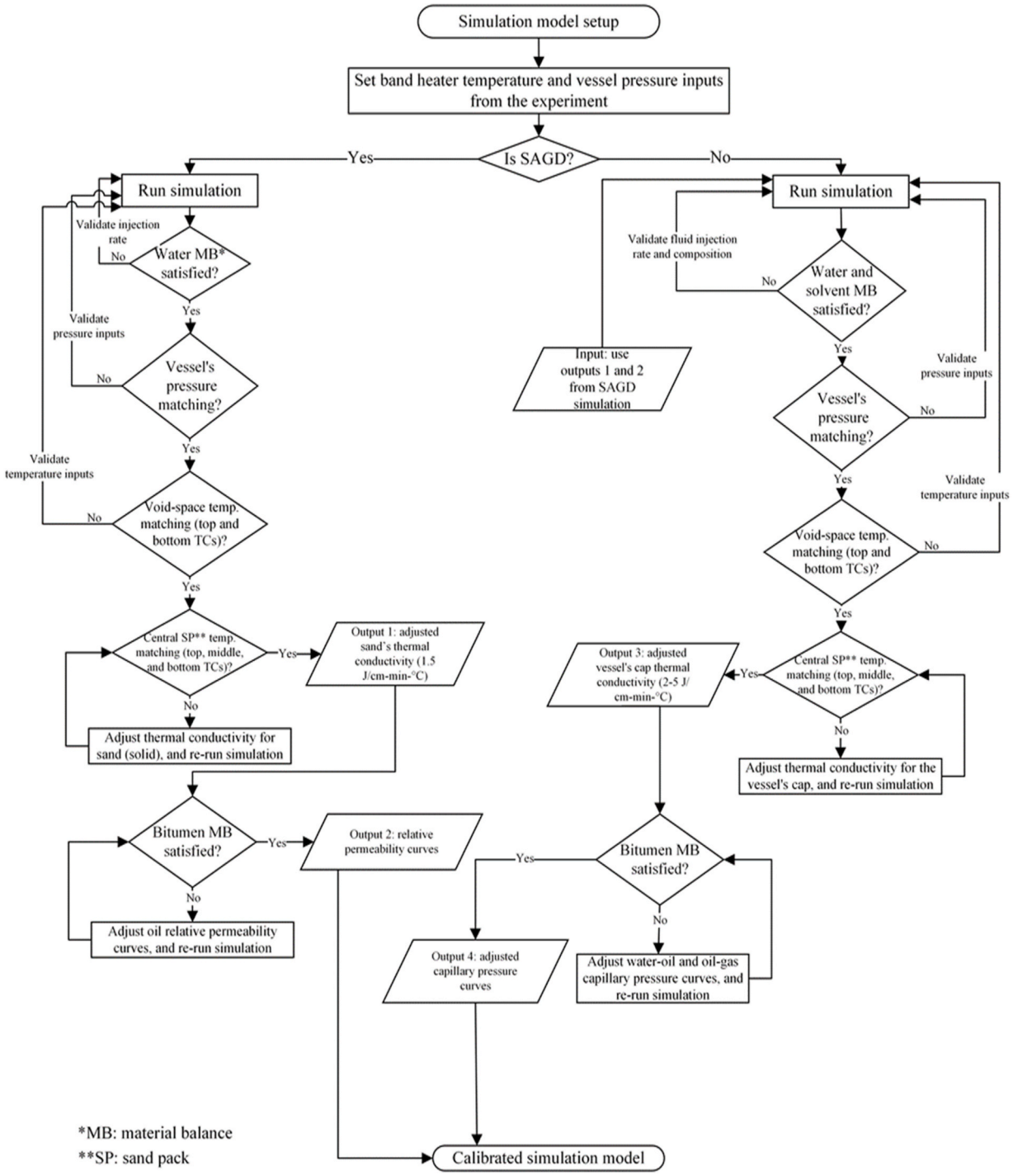

References

Al-Bahlani, A.M., Babadagli, T., 2009. SAGD laboratory experimental and numerical simulation studies: a review of current status and future issues. J. Petrol. Sci. Eng. 68 (3–4), 135–150. https://doi.org/10.1016/j.petrol.2009.06.011.

Amer, H., Sheng, K., Okuno, R., Al-Gawfi, A., Nakutnyy, P., 2024. A systematic comparison of solvents and their concentrations in bitumen gravity drainage under controlled thermodynamic conditions. Fuel 357 (A), 129723. https://doi.org/10.1016/j.fuel.2023.129723.

Baek, K.H., Sheng, K., Arguelles-Vivas, F.J., Okuno, R., 2019. Comparative study of oil-dilution capability of dimethyl ether and hexane as steam additives for steam-assisted gravity drainage. SPE Reservoir Eval. Eng. 22 (3), 1030–1048. https://doi.org/10.2118/187182-PA.

Bakhsh, A., Zhang, L., Wei, H., Shaikh, A., Khan, N., Khan, S., Shaoran, R., 2022. The approach of dimethyl ether-enhanced waterflooding (DEW) for oil recovery: a review. Arabian J. Geosci. 15 (6), 520. https://doi.org/10.1007/s12517-022-09747-3.

Butler, R.M., 1985. A new approach to the modelling of steam-assisted gravity drainage. J. Can. Petrol. Technol. 24 (3), 42–51. https://doi.org/10.2118/85-03-01.

Chai, M., Yang, M., Chen, Z., 2022. Systematical study on dimethyl ether as a renewable solvent for warm vapex and its significant implications for the heavy oil industry. Fuel 312, 122911. https://doi.org/10.1016/j.fuel.2021.12291.

Chernetsky, A., Masalmeh, S., Eikmans, D., et al., 2015. A novel enhanced oil recovery technique: experimental results and modelling workflow of the DME enhanced waterflood technology. In: Presented at the Abu Dhabi International Petroleum Exhibition and Conference, Abu Dhabi, 9–12 November. https://doi.org/10.2118/177919-MS. SPE-177919-MS.

Computer Modelling Group (CMG). STARS Version 2020 User's Guide. Computer Modelling Group, Calgary, Alberta, Canada..

deFernández, M.E.P., Calado, J.C., Zollweg, J.A., Streett, W.B., 1992. Vapor-liquid equilibria in the binary system dimethyl ether + n-butane from 282.9 to 414.5 K at pressures to 4.82 MPa. Fluid Phase Equil. 74, 289–302. https://doi.org/10.1016/0378-3812(92)85068-J.

Fleisch, T.H., Basu, A., Gradassi, M.J., Masin, J.G., 1997. Dimethyl ether: a fuel for the 21st century. Stud. Surf. Sci. Catal. 107, 117–125. https://doi.org/10.1016/S0167-2991(97)80323-0.

Gao, J., Okuno, R., Li, H.A., 2017. An experimental study of multiphase behavior for n-butane/bitumen/water mixtures. SPE J. 22 (3), 783–798. https://doi.org/10.2118/180736-PA, 10.2118/180736-PA.

Garcia-Sanchez, F., Laugier, S., Richon, D., 1987. Vapor-liquid equilibrium data for the methane-dimethylether and methane-diethylether systems between 282 and 344 K. J. Chem. Eng. Data 32, 211–215. https://doi.org/10.1021/je00048a024.

Haddadnia, A., Azinfar, B., Zirrahi, M., Hassanzadeh, Abedi J., 2018a. "Thermophysical Properties of Dimethyl ether/Athabasca Bitumen System" https://doi.org/10.1002/cjce.23009.

Haddadnia, A., Zirrahi, M., Hassanzadeh, H., Abedi, J., March, 2018b. Dimethylether-A promising solvent for ES-SAGD. In: Paper SPE-189741-MS Presented at the SPE Canada Heavy Oil Technical Conference. Canada, Calgary, Alberta. https://doi.org/10.2118/189741-MS.

Holldorff, H., Knapp, H., 1988. Binary vapor-liquid-liquid equilibrium of dimethyl ether—water and mutual solubilities of methyl chloride and water. Fluid Phase Equil. 44 (2), 195–209. https://doi.org/10.1016/0378-3812(88)80111-0.

Huron, M.J., Vidal, J., 1979. New mixing rules in simple equations of state for representing vapour-liquid equilibria of strongly non-ideal mixtures. Fluid Phase Equil. 3 (4), 255–271. https://doi.org/10.1016/0378-3812(79)80001-1.

Javanmard, H., Seyyedi, M., Jones, S.A., Nielsen, S.M., 2019. Dimethyl ether enhanced oil recovery in fractured reservoirs and aspects of phase behavior. Energy Fuel. 33, 10718–10727. https://doi.org/10.1021/acs.energyfuels.9b02600.

Keshavarz, M., Okuno, R., Babadagli, T., 2014. Efficient oil displacement near the chamber edge in ES-SAGD. J. Petrol. Sci. Eng. 118, 99–113. https://doi.org/10.1016/j.petrol.2014.04.007.

Keshavarz, M., Okuno, R., Babadagli, T., 2015. Optimal application conditions for steam-solvent coinjection. SPE Reservoir Eval. Eng. 18 (Number 1), 20–38. https://doi.org/10.2118/165471-PA.

Kumar, A., Okuno, R., 2016. A new algorithm for multiphase-fluid characterization for solvent injection. SPE J. 21 (5), 1688–1704. https://doi.org/10.2118/175123-PA. SPE-175123-PA.

Lee, S., Gogate, M., Kulik, C.J., 1995. Methanol-to-gasoline vs. DME-to-gasoline II. Process comparison and analysis. Fuel Sci. Technol. Int. 13, 1039–1057. https://doi.org/10.1080/08843759508947721.

Lee, Y.W., Lee, H.S., Jeong, M.S., Cho, J., Lee, K.S., 2021. Compositional modeling of dimethyl ether–CO2 mixed solvent for enhanced oil recovery. Appl. Sci. 11 (1), 406. https://doi.org/10.3390/app11010406.

Mahdizadeh, M., Eftekhari, A.A., Nick, H.M., 2019. Numerical modeling of water-soluble solvents for enhancing oil recovery in heterogeneous chalk reservoirs. J. Petrol. Sci. Eng. 175, 681–692. https://doi.org/10.1016/j.petrol.2018.12.083.

Nasr, T.N., Beaulieu, G., Golbeck, et al., 2003. Novel expanding solvent-SAGD process "ES-SAGD.". J. Can. Petrol. Technol. 42 (1), 13–16. https://doi.org/10.2118/03-01-TN.

Okuno, R., 2018. "Coinjection of Dimethyl Ether and Steam for Bitumen and Heavy Oil Recovery." https://doi.org/10.26153/tsw/3613. US Patent No. 10,125,591.

Outcalt, S.L., Lemmon, E.W., 2013. Bubble-point measurements of eight binary mixtures for organic Rankine cycle applications. J. Chem. Eng. Data 58, 1853–1860. https://doi.org/10.1021/je400251s.

Park, S.J., Han, K.J., Gmehling, J., 2007. Isothermal phase equilibria and excess molar enthalpies for binary systems with dimethyl ether at 323.15 K. J. Chem. Eng. Data 52, 1814–1818. https://doi.org/10.1021/je700174h.

Parsons, C., Chernetsky, A., Eikmans, D., et al., 2016. Introducing a novel enhanced oil recovery technology. In: Presented at the SPE Improved Oil Recovery Conference. https://doi.org/10.2118/179560-MS. Tulsa, 11 13 April. SPE-179560-MS.

Peters, E.J., 2012. Advanced Petrophysics: Geology, Porosity, Absolute Permeability, Heterogeneity, and Geostatistics, vol. 1. Greenleaf Book Group.

Pozo, M.E., Streett, W.B., 1984. Fluid phase equilibria for the system dimethyl ether/water from 50 to 220 C and pressures to 50.9 MPa. J. Chem. Eng. Data 29 (3), 324–329. https://doi.org/10.1021/je00037a030.

Pratama, R.A., Babadagli, T., 2020a. Reconsideration of steam additives to improve heavy-oil recovery efficiency: can new generation chemicals be a solution for steam-induced unfavorable wettability alteration? Energy Fuel. 34 (7), 8283–8300. https://doi.org/10.1021/acs.energyfuels.0c01406.

Pratama, Randy Agra, Babadagli, Tayfun, 2020b. Effect of temperature, phase change, and chemical additives on wettability alteration during steam applications in sands and carbonates. SPE Reservoir Eval. Eng. 23, 292–310. https://doi.org/10.2118/191188-PA.

Pratama, Randy Agra, Babadagli, Tayfun, 2021. Tertiary-recovery improvement of steam injection using chemical additives: pore-scale understanding of challenges and solutions through visual experiments. SPE J. 26, 1552–1571. https://doi.org/10.2118/200841-PA.

Ratnakar, R.R., Dindoruk, B., Wilson, L., 2016a. Experimental investigation of DME-water-crude oil phase behavior and PVT modeling for the application of DME-enhanced waterflooding. Fuel 182, 188–197. https://doi.org/10.1016/j.fuel.2016.05.096, 15 October.

Ratnakar, R.R., Dindoruk, B., Wilson, L., 2016b. Phase behavior experiments and PVT modeling of DME-brine-crude oil mixtures based on huron-vidal mixing rules for EOR applications. Fluid Phase Equil. 434, 49–62. https://doi.org/10.1016/j.fluid.2016.11.021, 25 February.

Robinson, D.B., Peng, D.Y., 1978. The characterization of the heptanes and heavier fractions for the GPA peng-robinson programs. In: Research Report RR-28. Gas Processors Association, Tulsa.

Rodriguez, F., Llamedo, M., Belhaj, H., Belhaj, A., 2022. Challenges associated with the acid gases production and capture in hydrocarbon reservoirs: a critical review of the Venezuelan cases. In: Presented at the SPE Thermal Well Integrity and Production Symposium. https://doi.org/10.2118/212146-MS. Banff, Alberta, Canada, 25 November. SPE-212146-MS.

Rodriguez, F., Llamedo, M., Belhaj, H., Mendoza, A., Elraies, K.A., 2023. Workflow of the in situ combustion EOR method in Venezuela: challenges and opportunities. ACS Omega 8 (31), 28060–28079. https://doi.org/10.1021/acsomega.2c08059.

Semelsberger, T.A., Borup, R.L., Greene, H.L., 2006. Dimethyl ether (DME) as an alternative fuel. J. Power Sources 156, 497–511. https://doi.org/10.1016/j.jpowsour.2005.05.082.

Sheng, K., Okuno, R., Wang, M., 2017. Water-soluble solvent as an additive to steam for improved SAGD. February 15 – 16. In: SPE Canada Heavy Oil Technical Conference. https://doi.org/10.2118/184983-MS. Calgary, Alberta, Canada.

Sheng, K., Okuno, R., Wang, M., 2018. Dimethyl ether as an additive to steam for improved steam-assisted gravity drainage. SPE J. 23 (4), 1201–1222. https://doi.org/10.2118/184983-PA.

Sheng, K., Okuno, R., Imran, M., Yamada, T., 2021. An experimental study of steam assisted gravity drainage. SPE J. 26 (3), 1515–1534. https://doi.org/10.2118/200867-PA.

Sheng, K., Amer, H., Liu, Y., Okuno, R., Al-Gawfi, A., Nakutnyy, P., Nakagawa, K., 2022a. A new experimental method for comparing solvents in steam-solvent coinjection for bitumen recovery under controlled thermodynamic conditions. J. Petrol. Sci. Eng. 213, 110377 https://doi.org/10.1016/j.petrol.2022.110377.

Sheng, K., Okuno, R., Al-Gawfi, A., Nakutnyy, P., Imran, M., Nakagawa, K., 2022b. An experimental study of steam-solvent coinjection for bitumen recovery using a large-scale physical model. SPE J. 27 (1), 381–398. https://doi.org/10.2118/205158-PA.

Soave, G., 1972. Equilibrium constants from a modified redlich-kwong equation of state. Chem. Eng. Sci. 27 (6), 1197–1203. https://doi.org/10.1016/0009-2509(72)80096-4.

Stewart, Robert A., Shaw, J.M., 2018. Interface renewal and concentration shock through sloughing: accounting for the dissonance between production models and measured outcomes for solvent–assisted bitumen–production processes. SPE Reservoir Eval. Eng. 21, 174–186. https://doi.org/10.2118/186108-PA.

Venkatramani, A.V., Okuno, R., 2015. Characterization of water-containing reservoir oil using an EOS for steam injection processes. J. Nat. Gas Sci. Eng. 26, 1091–1106. https://doi.org/10.1016/j.jngse.2015.07.036.

Yang, S., Nie, Z., Wu, S., Li, Z., Wang, B., Wu, W., Chen, Z., 2021a. A critical review of reservoir simulation applications in key thermal recovery processes: lessons, opportunities, and challenges. Energy Fuel. 35 (9), 7387–7405. https://doi.org/10.1021/acs.energyfuels.1c00249.

Yang, M., Chai, M., Qi, R., Chen, Z., Zhang, L., Yu, X., 2021b. Dimethyl ether as a novel solvent for bitumen recovery: mechanisms of improved mass transfer and Energy Efficiency. SPE J. 27 (2), 1321–1340. https://doi.org/10.2118/208615-pa.

Zhao, X., Zhou, F., Chen, Z., Zan, J., Liang, T., Zhang, M., 2023. Dynamic monitoring and enhanced oil recovery evaluation of the water flooding process of liquid nanofluids in tight reservoirs. Energy Fuel. 37 (6), 4256–4266. https://doi.org/10.1021/acs.energyfuels.2c03936.